Surface Science 603 (2009) 1161–1167

Contents lists available at ScienceDirect

Surface Science

journal homepage: www.elsevier.com/locate/susc

Formation and structure of a ($\sqrt{19} \times \sqrt{19}$)R23.4°-Ge/Pt(1 1 1) surface alloy

Chih-Sung Ho [a], Santanu Banerjee [b], Matthias Batzill [c], David E. Beck [d], Bruce E. Koel [e,*]

[a] Department of Chemical Engineering, Tunghai University, Taichung 40744, Taiwan
[b] Department of Physics, Tougaloo College, Tougaloo, MS 39174, USA
[c] Department of Physics, University of South Florida, Tampa, FL 33620-5700, USA
[d] Asylum Research, 3-4 Shaochuan Street, Kaohsiung City 80441, Taiwan, ROC
[e] Department of Chemistry and Center for Advanced Materials and Nanotechnology, Lehigh University, 6E. Packer Ave., Bethlehem, PA 18015-3172, United States

ARTICLE INFO

Article history:
Received 2 October 2008
Accepted for publication 22 January 2009
Available online 30 January 2009

Keywords:
Germanium
Platinum
Alloy
Low energy electron diffraction
Scanning tunneling microscopy
X-ray photoelectron diffraction
Low energy ion scattering
Alkali ion scattering

ABSTRACT

An ordered ($\sqrt{19} \times \sqrt{19}$)R23.4°-Ge/Pt(1 1 1) surface alloy can be formed by vapor depositing one-monolayer Ge on a Pt(1 1 1) substrate at room temperature and subsequently annealing at 900–1200 K. The long-range order of this structure was observed by low energy electron diffraction (LEED) and confirmed by scanning tunneling microscopy (STM). The local structure and alloying of vapor-deposited Ge on Pt(1 1 1) at 300 K was investigated by using X-ray Photoelectron Diffraction (XPD) and low energy alkali ion scattering spectroscopy (ALISS). XPS indicates that Ge adatoms are incorporated to form an alloy surface layer at ~900 K. Results from XPD and ALISS establish that Ge atoms are substitutionally incorporated into the Pt surface layer and reside exclusively in the topmost layer, with excess Ge diffusing deep into the bulk of the crystal. The incorporated Ge atoms at the surface are located very close to substitutional Pt atomic positions, without any corrugation or "buckling". Temperature Programmed Desorption (TPD) shows that both CO and NO adsorb more weakly on the Ge/Pt(1 1 1) surface alloy compared to that on the clean Pt(1 1 1) surface.

1. Introduction

Platinum is well known as a catalyst with high activity for hydrogenation and dehydrogenation [1]. Addition of a second metal component usually enhances the activity, selectivity, and/or lifetime of the catalyst. For example, catalysts containing Pt–Ge intermetallic compounds (ordered alloys) have a much lower activity for the hydrogenation of 1,3-butadiene than that of catalysts of pure Pt, with the activity decreasing with increasing Ge concentration, but they have a much higher selectivity to butene products because of weaker adsorption of butenes on the alloy surfaces than on pure Pt [1,2]. In other examples as well, such as the conversion of butane to aromatic hydrocarbons, lowering the dehydrogenation activity helps control the formation of coke on the Pt–Ge alloy surfaces and this contributes to a longer catalyst lifetime [1].

One can use model systems to investigate aspects of this catalysis, either with bulk-crystal alloy surfaces or surface alloys formed by vapor deposition of one metal on another. Advantages of using surface alloys rather than bulk alloys can be higher thermal and chemical stability, and the possibility that one can grow surface alloy structures that do not exist in bulk phases. Some recent examples of ordered, bimetallic Pt surface alloys that have been formed and studied include the (2 × 2)-Sn/Pt(1 1 1) and ($\sqrt{3} \times \sqrt{3}$)R30°-Sn/Pt(1 1 1) [3], and c(2 × 2)-Sn/Pt(1 0 0) and ($3\sqrt{2} \times \sqrt{2}$)R45°-Sn/Pt(1 0 0) [4] structures. The chemical properties of these intermetallic compounds are quite different from those of pure Pt [5–10]. Moreover, the electronic structure at Pt sites is expected to be perturbed and STM has provided new insight into "local effects" on the electronic structure of such alloy surfaces [11].

Bimetallic surfaces formed by vapor depositing Ge on a Pt(1 1 1) substrate have been studied by Fukutani et al. [12,13]. LEED studies show that only disordered structures are formed when alloying is induced by repeating cycles of deposition of a few monolayers of Ge and subsequent annealing at 1100 °C [13]. More recently, it was reported that an ordered (5 × 5)-Ge/Pt(1 1 1) surface alloy could be formed by depositing two monolayers of Ge on Pt(1 1 1) and then heating to 1300 K, based on STM investigations [12]. Both studies reported that the Ge surface concentration is very small, 10% at most. However, these dilute Ge–Pt surface alloys have different chemical properties and electronic structure compared to that of pure Pt(1 1 1) [12–14].

Our interest in this system was stimulated by this report that an ordered Ge–Pt alloy could be grown. We investigated this system further using LEED, XPS, XPD, ALISS, and STM in order to learn more about the 3D structure of the alloy produced in this manner. Because the atomic radius of Ge (1.22 Å) is 12% smaller than that of Pt (1.38 Å), an inward buckling of Ge atoms in the top Pt atomic layer would be predicted based on the previous identification of

* Corresponding author. Tel.: +610 758 5650; fax: +610 758 6536.
E-mail address: brk205@lehigh.edu (B.E. Koel).

0039-6028/$ - see front matter © 2009 Elsevier B.V. All rights reserved.
doi:10.1016/j.susc.2009.01.028

a linear relationship between buckling distance and lattice mismatch for *fcc* metals [15–17]. Our results differ somewhat from the previous studies cited above, and we found that a $(\sqrt{19} \times \sqrt{19})$R23.4°-Ge/Pt(1 1 1) surface alloy is formed upon annealing a 1-ML Ge film to 900–1200 K. The Ge concentration at this alloy surface is very dilute, only 5.3%. This finding is quite exciting because the Ge is much more dilute than the alloyed Sn found in previous studies of Sn–Pt surface alloys [3,4]. Thus, this alloy contains much larger Pt ensembles that are available for reactions and offers new opportunities for further developing structure–reactivity relationships at alloy surfaces.

2. Experimental methods

The experiments were conducted in an ultrahigh vacuum (UHV) chamber and apparatus that is essentially the same as shown and described previously [18,19]. The chamber is a two-level UHV system with a base pressure in the low 10^{-10}-Torr range during experiments. The chamber was equipped with an UTI 100C quadrupole mass spectrometer (QMS) for temperature programmed desorption (TPD) and four-grid electron optics for low energy electron diffraction (LEED) on the top level. The bottom level contains a dual Al/Mg X-ray source, Colutron ion gun to provide a monoenergetic and collimated ion source, ion gun for Ar^+-ion sputtering, and Perkin–Elmer Model 10-360 spherical capacitor analyzer (SCA) for X-ray photoelectron spectroscopy (XPS), X-ray photoelectron diffraction (XPD), and low energy ion scattering (LEIS), and alkali ion scattering spectroscopy (ALISS). The SCA is mounted at a fixed scattering angle θ of 144° for LEIS and ALISS. Several ports were utilized for gas dosing and metal deposition at convenient positions.

A custom sample holder capable of both resistive and electron-beam heating was attached to a VG Omniax manipulator. A Pt(1 1 1) single crystal sample (Atomergic Chemetals Corp.) was used, which was 10-mm diameter and 1.0-mm thick and was oriented to within +/−0.5°. The crystal was held on the sample holder by two W wires that fit into slots at the edge of the crystal. A chromel/alumel thermocouple that was spot-welded to the edge of the crystal was used to monitor the sample temperature. The manipulator had three translational (*X*, *Y*, and *Z* axes) and two rotational (polar and azimuthal angles) degrees of freedom. Both rotational motions were controlled by stepping motors that could be operated either manually or programmed through a computer. The accuracy of our measurements of the polar angle (ψ for XPD and ψ for ALISS), azimuthal angle ϕ, and scattering angle θ are ±0.5°, ±1°, and ±0.5°, respectively. The Pt(1 1 1) crystal was cleaned by a standard procedure involving cycles of Ar^+-ion sputtering, heating in an oxygen ambient and annealing to high temperatures in vacuum [3,7,18,20]. The cleanliness of the surface was checked by XPS and LEED which showed a sharp p(1 × 1) pattern.

The Ge doser was made by placing high-purity Ge metal pieces (ESPI, 6N, 16 mesh) inside an evaporation boat constructed of Ta. Ge deposition was performed by resistively heating the Ta boat to evaporate Ge atoms through a small pinhole in the boat cover onto the crystal surface. The doser temperature was monitored by a chromel/alumel thermocouple spot-welded to the center of the rear side of the Ta boat. As described later, the Ge coverage Θ_{Ge} was evaluated by using CO TPD. In this paper, Θ_{Ge} = 1 monolayer is defined with respect to the Pt surface atom density corresponding to 3.01×10^{15} atoms/cm^2.

All XPD and ALISS measurements reported in this paper were taken on the ordered $(\sqrt{19} \times \sqrt{19})$R23.4°-Ge/Pt(1 1 1) surface alloy created by depositing one-monolayer Ge onto the Pt(1 1 1) surface at room temperature and subsequently annealing at 1000 K. This structure was confirmed both by LEED and STM. No other conditions of initial Ge coverage were investigated.

The polar angle ψ in ALISS is defined with respect to the crystal surface, with ψ = 0° corresponding to incident ions parallel to the surface. The angle between the ion source and the SCA is 36°. Therefore, the ion scattering angle θ is fixed at 144°. The Na^+-ion source was a thermal emission, aluminosilicate cathode (SPECTRA-MAT, INC.) which had been ion exchanged with sodium ions. This type of ion emitter material has an advantage that it does not readily react with the atmosphere. The ALISS spectra for the Ge/Pt(1 1 1) alloy were measured and analyzed in a manner similar to that in our previous Zn/Pt(1 1 1) study [18]. The Na^+-ion source operating conditions and signal scan parameters were also identical to those reported in Ref. [18].

Following the traditional convention in XPD, the polar angle ψ is defined oppositely to that in ALISS with respect to the surface normal, such that ψ = 0° corresponds to the analyzer located perpendicular to the surface. The angle between the X-ray source and the analyzer is fixed at 42.5°. An Al–Kα X-ray source was used for both XPS and XPD scans. The X-ray source operating conditions and signal scan parameters were identical to those reported in Ref. [18], except for the Ge $2p_{3/2}$ scan range which was from 1230 to 1205 eV.

3. Results and discussion

3.1. Evaluation of 1-ML Ge coverage

Fig. 1 shows a CO "uptake" curve obtained from the integrated area under CO desorption peaks in TPD obtained for increasing amounts of Ge deposited on the Pt(1 1 1) surface at 300 K. CO TPD curves were obtained by exposing CO to the Ge/Pt(1 1 1) surface at 300 K, forming a saturation coverage of CO, and then thermally desorbing CO from the surface. CO TPD was performed from 300 to 600 K, where all deposited Ge atoms still remain at the Pt(1 1 1) surface and no alloying occurs (we will address this further during a discussion of the alloying process later). XPS was used to monitor the amount of deposited Ge by using the Ge $2p_{3/2}$ peak. The intensity of this peak was obtained by using the peak height after subtracting a background curve and subsequently normalizing by the clean Pt 4f peak intensity. Because CO adsorbs only on Pt [14], the CO TPD area decreases as the amount of deposited Ge increases. We define the point where one-monolayer of deposited Ge covers the Pt(1 1 1) surface as the change in slope of this curve, as shown by the arrow. The CO TPD area never fully attenuated to zero even when the Pt(1 1 1) surface was covered by more

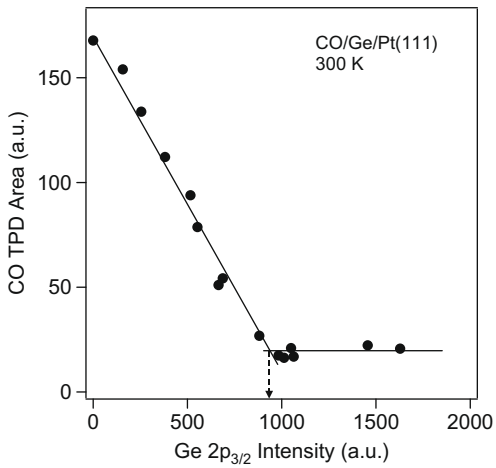

Fig. 1. Determination of the Ge monolayer coverage based on an evaluation of the CO TPD area as a function of the Ge $2p_{3/2}$ XPS intensity for Ge deposited on Pt(1 1 1) at 300 K. The arrow denotes 1-ML Ge.

than 1-ML Ge atoms. This is attributed to CO desorption from the edge and back of the crystal where no Ge was deposited. The Ge $2p_{3/2}$: Pt 4f ratio in XPS ranged from 0 to 0.17 as the amount of Ge deposited increased from zero to 1 ML.

3.2. Alloying process

The thermal stability of this Ge monolayer and the alloying process was investigated by varying the annealing temperature subsequent to the deposition of 1-ML Ge on the Pt(1 1 1) surface at 300 K. Fig. 2 shows the measured Ge $2p_{3/2}$ intensity in XPS versus crystal annealing temperature. The Ge intensity did not significantly change between 300 and 800 K, but it did decrease for annealing temperatures between 800 and 900 K. This implies that most of the Ge adlayer remains at the Pt(1 1 1) surface until annealing temperatures above 800 K. LEED showed no features, not even the 1×1 clean Pt(1 1 1) spots, at temperatures at or below 800 K. However, an ordered, *fcc*(1 1 1)-($\sqrt{19} \times \sqrt{19}$)R23.4° two-domain pattern was observed after annealing at 900 K. This ordered structure was quite stable thermally, and no changes in the LEED pattern (or in STM images) occurred upon further annealing up to 1200 K. For the sake of brevity, we refer to this surface structure (due to an alloy as established below) as the $\sqrt{19}$ alloy throughout the rest of this paper.

While the surface unit cell was unchanged, the Ge $2p_{3/2}$ intensity decreased during heating from 900 to 1200 K. We show later that the Ge concentration in this surface alloy is much lower than the surface Ge concentration before annealing, i.e., one-monolayer. This implies that Ge atoms leave the surface upon heating from 900 to 1200 K, either by desorbing from the surface or diffusing deep into the substrate. XPD and ALISS results presented later show that no Ge atoms exist in the several atomic layers closest to the surface except for the topmost layer after alloying. Because Ge was detected by XPS following Ar^+-ion bombardment and annealing, and it required several repeated cycles of sputtering-annealing to get a clean Pt(1 1 1) surface again, we believe that annealing causes at least a significant amount of Ge atoms to diffuse deep into the bulk. Ge desorption cannot be ruled out because no experiment was performed to detect Ge desorption from the surface during heating. The gradual decrease in the Ge $2p_{3/2}$ intensity during heating from 900 to 1200 K indicates that Ge atoms gradually diffuse deeper into the crystal and out of the XPS probe depth or desorb as the annealing temperature is increased.

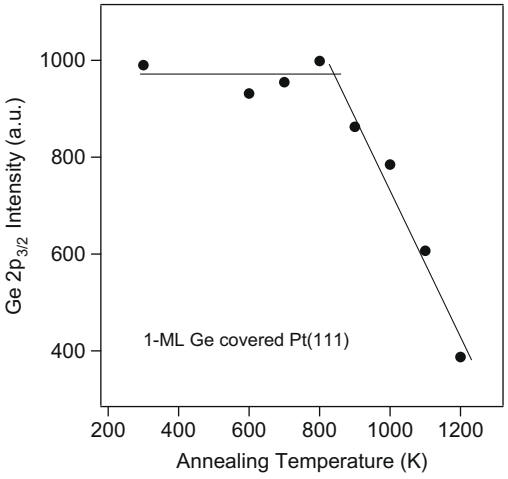

Fig. 2. Ge $2p_{3/2}$ XPS intensity for a 1-ML Ge film deposited on Pt(1 1 1) after annealing to several temperatures. The decrease in the Ge $2p_{3/2}$ intensity between 800 and 1200 K indicates that alloying takes place within this temperature range.

3.3. LEED and STM

Fig. 3a provides the LEED image observed after annealing one-monolayer Ge on Pt(1 1 1) at 1000 K. The circled spots correspond to the *fcc*(1 1 1)-p(1×1) pattern. A schematic drawing of a *fcc*(1 1 1)-($\sqrt{19} \times \sqrt{19}$)R23.4° reciprocal lattice with two-domains [21] is shown in Fig. 3b, which precisely accounts for the spot location and symmetry of this LEED image. The unit cells for the two different domains are shown as solid and dashed lines. Fig. 3c is a real-space model for the ($\sqrt{19} \times \sqrt{19}$)R23.4°-Ge/Pt(1 1 1) structure assuming a primitive unit cell formed by Ge atoms, with Ge atoms occupying substitutional lattice sites for surface Pt atoms. Two-domains are possible, and the angle between the two unit cells can be calculated to be 13.2°. We will show later the ALISS

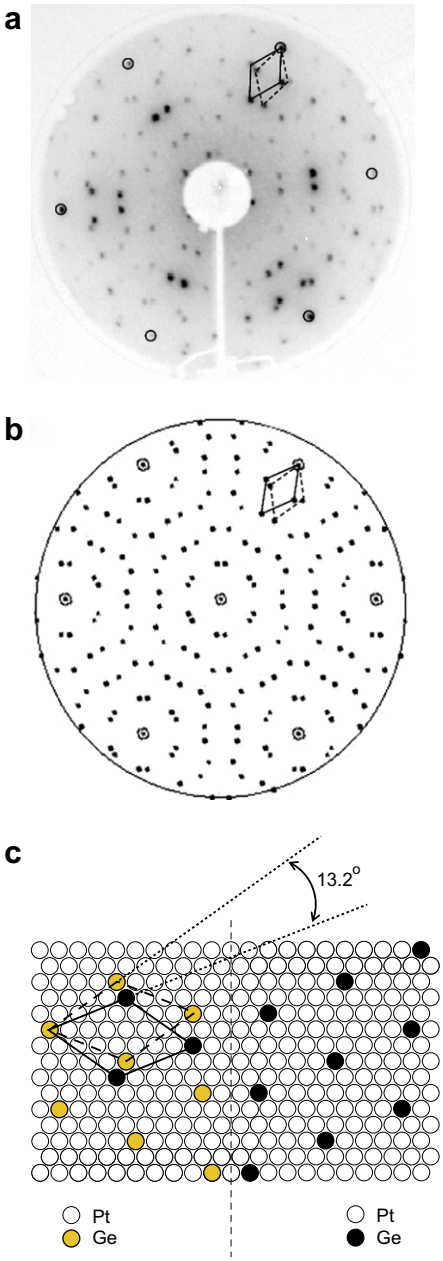

Fig. 3. (a) Photograph of the LEED image obtained at a beam energy of 70 eV for 1-ML Ge deposited Pt(1 1 1) at 300 K after annealing to 1000 K. (b) A schematic drawing of a two-domain *fcc*(1 1 1)-($\sqrt{19} \times \sqrt{19}$)R23.4° reciprocal lattice and the associated unit cells. (c) Real-space model proposed for a two-domain *fcc*(1 1 1)-($\sqrt{19} \times \sqrt{19}$)R23.4° surface alloy.

data that establish that this structure is due to incorporated Ge atoms rather than Ge adatoms in the overlayer on Pt(1 1 1).

Because the ($\sqrt{19} \times \sqrt{19}$)R23.4° unit cell is such a large structure, it is important to determine if the unit cell is "primitive", i.e., if there is only one Ge atom within each unit cell. If the unit cell is non-primitive, then the Ge concentration should be $(5.3 \times n)$% where n represents the number of Ge atoms within the unit cell. STM images can greatly aid in the determination of the concentration of Ge at the surface, because of the chemical contrast that exists between Ge and Pt atoms. This contrast arises from the different I–V characteristics between Ge and Pt. Fig. 4a is the STM image obtained after the one-monolayer Ge film on Pt(1 1 1) was annealed to 1000 K. Arrows show the main crystallographic directions. Bright spots were observed arranged at the corners of a ($\sqrt{19} \times \sqrt{19}$)R23.4° unit cell. These bright spots are attributed to Ge atoms alloyed at the surface of the Pt(1 1 1) crystal. The basis vector length of 12.1 Å for the Ge superstructure is $\sqrt{19}$ times the unit-vector length of 2.77 Å for Pt. The most direct interpretation of this image is that it corresponds to one Ge atom within each $\sqrt{19}$ unit cell, and a Ge concentration of 5.3%. ALISS measurements discussed later independently and quantitatively determine that this is the Ge concentration in the topmost layer of this alloy. This validates our interpretation of the STM image, and we believe that the odd shape of the bright spots is due to tip effects. This Ge concentration also can be used as a reference for calculating concentrations of non-ordered, dilute alloys by comparing the XPS or AES intensities of such surfaces to those from the $\sqrt{19}$ alloy. This calibration can be used also for alloys other than Ge–Pt, using appropriate sensitivity factors, and this has been done for alloys in the Zn/Pt(1 1 1) [18] and Cu/Pt(1 1 1) [18] systems.

The STM image in Fig. 4b for this $\sqrt{19}$ alloy surface shows a large domain boundary between two-domains. The angle between the two lines indicated along the white spots (Ge atoms) in the two-domains is 13.2°, identical to the calculated value for the *fcc*(1 1 1)-($\sqrt{19} \times \sqrt{19}$)R23.4° two-domain structure. This is also consistent with the interpretation of the LEED pattern.

Fig. 4c depicts a real-space model for the ($\sqrt{19} \times \sqrt{19}$)R23.4°-Ge/Pt(1 1 1) surface alloy which corresponds to the STM image in Fig. 4a. Thus, the 2D structure of this surface appears to be resolved. Now, we discuss additional XPD and ALISS measurements in order to add information about the 3D structure, and specifically address whether the Ge atoms are coplanar with the Pt atoms in the topmost layer.

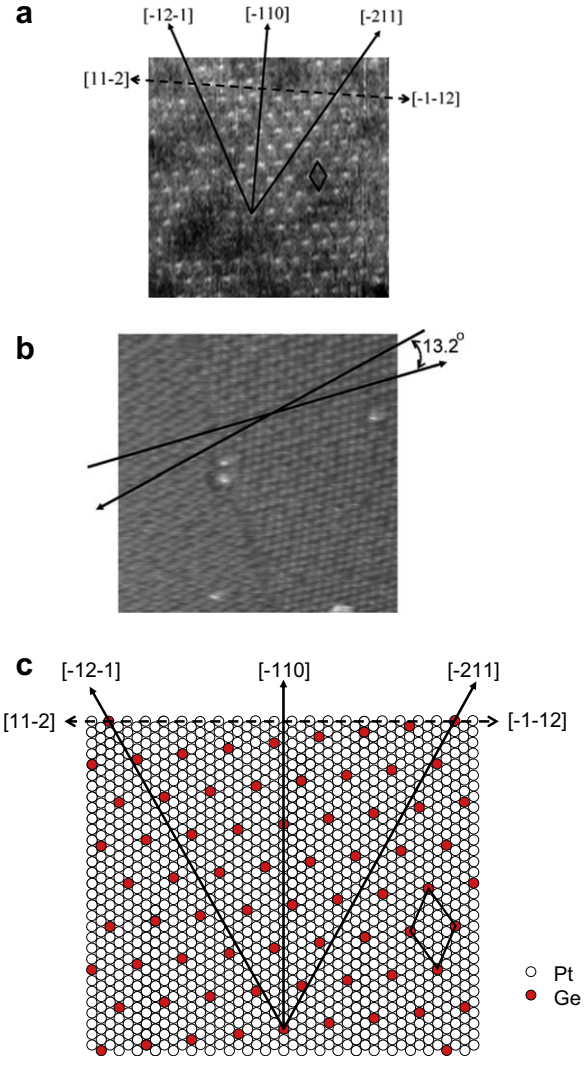

Fig. 4. (a) STM image (15×15 nm^2) of the $\sqrt{19}$ Ge–Pt(1 1 1) surface alloy obtained with −200-mV sample bias and 0.2-nA tunneling current. The solid line indicates the unit cell of alloyed Ge atoms. (b) STM image (30×30 nm^2) showing two-domains of the $\sqrt{19}$ Ge–Pt(1 1 1) surface alloy obtained using −500-mV sample bias and 0.16-nA tunneling current. (c) Model of the ($\sqrt{19} \times \sqrt{19}$)R23.4°-Ge/Pt(1 1 1) surface alloy corresponding to the STM image in (a).

3.4. XPD

Fig. 5a provides XPD polar scans along the [−1 2 −1] azimuth for a 1-ML Ge film deposited on Pt(1 1 1) at 300 K. The Pt 4f polar scan

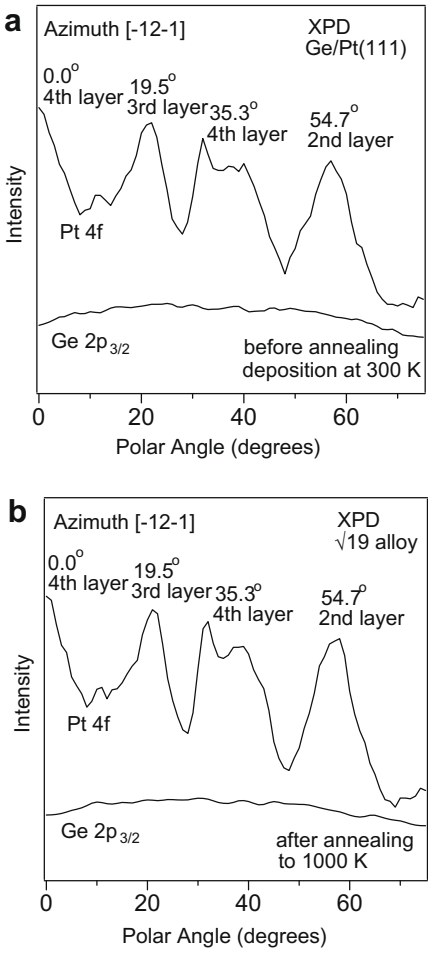

Fig. 5. (a) XPD polar scans along the [−1 2 −1] azimuth for 1-ML Ge deposited on Pt(1 1 1) at 300 K before annealing. (b) XPD polar scans along the [−1 2 −1] azimuth for 1-ML Ge deposited on Pt(1 1 1) at 300 K after annealing at 1000 K and forming the $\sqrt{19}$ alloy.

has four forward-scattering peaks near ψ = 0, 19.5, 35.3, and 54.7°. These peaks correspond to specific internuclear directions that define the origin of each peak to contributions from the 4th, 3rd, 4th, and 2nd-layer Pt atoms, respectively [18]. In the Ge $2p_{3/2}$ polar scan, the Ge $2p_{3/2}$ peak in XPS was observed at every polar angle from ψ = 0°–75°, but with no enhanced diffraction peaks. This establishes that the deposited Ge atoms are located only at the topmost layer. XPD polar scans along the [−1 2 −1] azimuth for the $\sqrt{19}$ alloy, formed by annealing this film to 1000 K, are shown in Fig. 5b. Both of the Pt 4f and Ge $2p_{3/2}$ polar scans are similar to the respective scans obtained before annealing. This shows that there is no appreciable amount of Ge in the near-surface atomic layers except for the topmost layer after the $\sqrt{19}$ alloy is formed. This indicates that excess Ge atoms diffuse into deeper (>4th) layers or desorb when alloying occurs.

3.5. ALISS

ALISS is a powerful tool that can be used to measure the three-dimensional atomic structure of a single crystal surface. In a large angle scattering, if the incident beam is at a grazing angle, the incident beam can only impact the first atom in a chain along a given direction, and there is no scattering from other atoms in the chain in the first-layer because of the "shadow cone" effect. Thus, no scattered ions are measured until the incident angle increases to a certain value at which the atoms behind the first atom emerge from the "shadow cones" [4,15,17]. That particular angle usually is called the "critical angle" for the first-layer. Similarly there are critical angles for the deeper layers when the incident angle reaches high values. Accounting for the azimuthal dependence and knowledge of the size of the shadow cone, the scattering can provide a 3D evaluation of distances between atoms in the surface region.

Figs. 6–8 show polar angle scans for 1-keV Na^+-ions scattered from Pt atoms at the surface of clean Pt(1 1 1) and the $\sqrt{19}$ Ge/Pt(1 1 1) alloy along the [−1 2 −1], [−2 1 1], and [−1 1 0] azimuths, respectively. The scans from clean Pt(1 1 1) and the $\sqrt{19}$ alloy along the long azimuth [−1 2 −1] in Fig. 6 are similar. For polar angles ψ below 10°, there is almost no Pt scattering feature. The peaks near 20° are due to first-layer Pt scattering and peaks at a higher angle near 58° are due to second-layer Pt scattering [17,18,22]. Such shadow cone effects [18,23,24] can be used to distinguish between Ge adatoms and Ge atoms incorporated within the top Pt layer. Because the concentration of Ge is very dilute (5.3%) for the $\sqrt{19}$ alloy, the Pt first-layer scattering peak of the $\sqrt{19}$ alloy is not very sensitive to the location of the Ge adatoms. As discussed below, the Ge polar angle scans are much more important for determining the alloying geometry of Ge atoms.

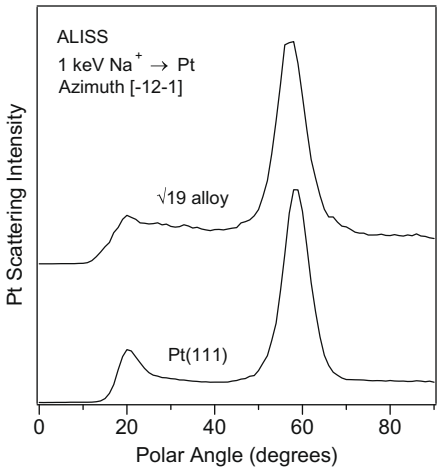

Fig. 6. Polar angle scans for 1-keV Na^+-ions scattered from Pt atoms for clean Pt(1 1 1) and the $\sqrt{19}$ alloy along the long azimuth [−1 2 −1].

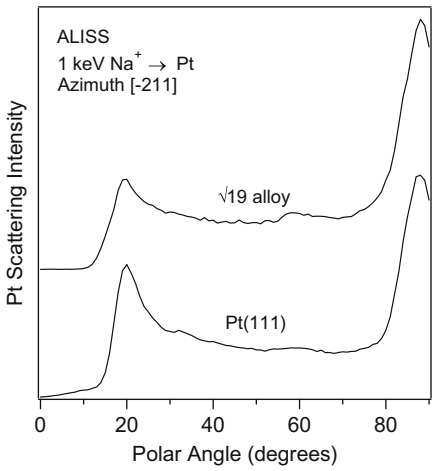

Fig. 7. Polar angle scans for 1-keV Na^+-ions scattered from Pt atoms for clean Pt(1 1 1) and the $\sqrt{19}$ alloy along the long azimuth [−2 1 1].

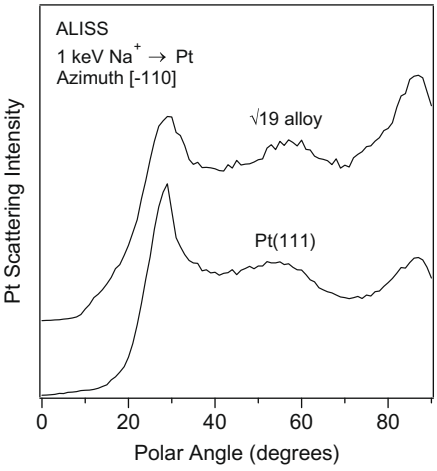

Fig. 8. Polar angle scans for 1-keV Na^+-ions scattered from Pt atoms for clean Pt(1 1 1) and the $\sqrt{19}$ alloy along the short azimuth [−1 1 0].

The scans shown in Fig. 7 for clean Pt(1 1 1) and the $\sqrt{19}$ alloy along another long azimuthal direction [−2 1 1] are almost unaltered, similar to that along the [−1 2 −1] direction. The peaks near 20° are due to first-layer Pt scattering and peaks at a higher angle near 88° are due to third-layer Pt scattering [17,18,22], and there is no second-layer Pt scattering feature. This latter feature enables the [−1 2 −1] azimuth to be distinguished from the [−2 1 1] azimuth [18].

Fig. 8 shows scans for clean Pt(1 1 1) and the $\sqrt{19}$ alloy along the short azimuth [−1 1 0]. These also show no significant differences between the two scans. However, the lower angle peaks near 29° that originate from first-layer Pt scattering occur at higher polar angle than those along the long azimuths [−1 2 −1] and [−2 1 1]. The distance between each Pt atom and its nearest neighbor atoms is larger along the long azimuth than along the short azimuth, as shown Fig. 4c. A higher angle (ψ = 29°) is necessary therefore to let the first-layer atoms emerge out of the shadow cones created by their neighbors along the short azimuth than along the long azimuth (ψ = 20°) [3,17,18].

Fig. 9 shows polar angle scans for 1-keV Na^+-ions scattered from Ge atoms for the $\sqrt{19}$ alloy along the [−12−1], [−211], and [−110] azimuths, respectively. Ge scattering along the [−12−1] azimuth has the same first-layer enhanced peak position near $\psi = 20°$ as that for Pt scattering from clean Pt(111) and the $\sqrt{19}$ alloy. This establishes that Ge atoms replace topmost layer Pt atoms and are incorporated into the Pt surface to form an alloy rather than occupying adatom sites to form an overlayer. If Ge adatoms formed an overlayer, the Ge first-layer enhanced scattering peak would be at a much lower angle. This is because the spacing between a Ge adatom and its nearest neighboring Ge adatom along the [−12−1] azimuth is very large in a $\sqrt{19}$ structure which has very dilute Ge concentration of 5.3%. From one Ge atom to the next, there are 18 Pt atoms between them. Similarly, along the [−211] and the [−110] azimuths, there are also 18 Pt atoms between one Ge atom and the next. Also, one can notice that along the [−12−1] azimuth, there is no Ge second-layer scattering feature at 58°, consistent with the conclusion reached from analyzing the Ge $2p_{3/2}$ XPD polar scans.

Ge first-layer scattering along the [−211] and [−110] azimuths is similar to that of Pt first-layer scattering from clean Pt(111) and the $\sqrt{19}$ alloy. This also supports the conclusion that Ge atoms substitutionally incorporate into the topmost layer of Pt atoms rather than form an overlayer. Ge scattering along the [−211] azimuth has no third-layer scattering peak near 88°, and this is different from Pt scattering from clean Pt(111) and the $\sqrt{19}$ alloy. This establishes that Ge in the alloy is not present in the third-layer, confirming the result deduced from the Ge $2p_{3/2}$ XPD polar scan. Ge forms a single-layer thick, surface alloy with no appreciable concentration of Ge in the second or third-layers of the substrate.

ALISS data can be used to quantitatively determine the Ge concentration in the topmost layer of the alloy. For $\psi = 55°$, along the [−211] azimuth, there is only first-layer scattering observed. Thus, the Ge concentration can be determined using the ion scattering intensities measured for Ge and Pt at these angles for the Ge/Pt(111) alloy and the following relationship:

$$C_{Ge} = \frac{I_{Ge}/S_{Ge}}{I_{Ge}/S_{Ge} + I_{Pt}/S_{Pt}} \quad (1)$$

The sensitivity factors were evaluated using ALISS spectra taken at the same conditions for clean Pt(111) and a thick Ge film (where no Pt scattering was observed). This determined that $S_{Pt}/S_{Ge} = 1.8$, and that $C_{Ge} = 0.056$ ML for the $(\sqrt{19} \times \sqrt{19})$R23.4°-Ge/Pt(111) surface alloy.

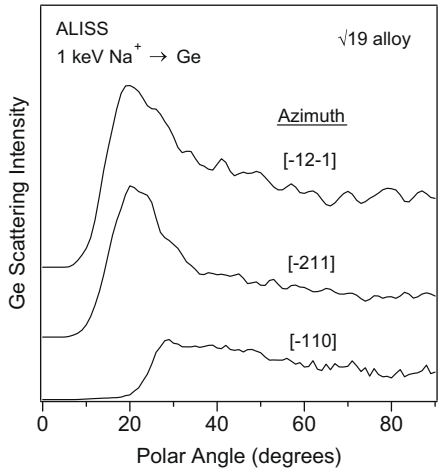

Fig. 9. Polar angle scans for 1-keV Na^+-ions scattered from Ge atoms for the $\sqrt{19}$ alloy along three different azimuths [−12−1], [−211], and [−110].

3.6. Critical angles in ALISS and the buckling distance

The critical angle ψ_c in an ALISS polar scan is usually defined as that angle which has an intensity of 90% of the scattering peak maximum [4,15,17]. The first-layer scattering features of Pt (from clean Pt(111) and the $\sqrt{19}$ alloy) and Ge (from the $\sqrt{19}$ alloy) along the [−211] azimuthal direction are shown in Fig. 10. The critical angles ψ_c are assigned at 18.7, 18.4, and 18.7° for each scan, respectively. These values should be regarded as identical within experimental error. Measurements along the other two azimuthal directions [−12−1] and [−110] gave similar results. Comparing these values of the critical angle ψ_c can determine the relative position of Ge and Pt atoms [3,4,15–17,22]. In this dilute alloy, all of the Ge atoms are surrounded by Pt atoms and far away from the nearest neighbor Ge atom. Therefore, we can assume that the shadow cones are produced by the scattering from Pt in both Pt and Ge cases. If Ge atoms directly substitute for the Pt atoms in the first-layer, then the critical angles of Pt and Ge scattering should be the same. Otherwise, if the alloyed Ge atoms were displaced vertically or buckled outward relative to the Pt atoms in the surface plane, the critical angle of the Ge scattering peak would occur at a lower position than that of the Pt scattering peak. Or, if Ge atoms are buckled inward from the Pt surface plane, the critical angle for the Ge scattering peak would be at a higher position than that of the Pt scattering peak. The determination of no significant shift between these two critical angles establishes that the average position of first-layer Ge atoms is coplanar with the Pt(111) surface without any buckling (≤0.01 Å). The uncertainty in this measurement is on the order of 0.084 Å for a shift of 1.0° for ψ_c in the [−211] azimuth [15].

This deviates from our prediction because there is a 12% radius mismatch between Ge and Pt atoms and an inward buckling of Ge atoms in the top Pt atomic layer is predicted [15–17]. Since the atomic radius of Ge (1.22 Å) is smaller than that of Pt (1.38 Å), perhaps a strain relief is not necessary. Previous observations of a linear relationship between the lattice mismatch and surface

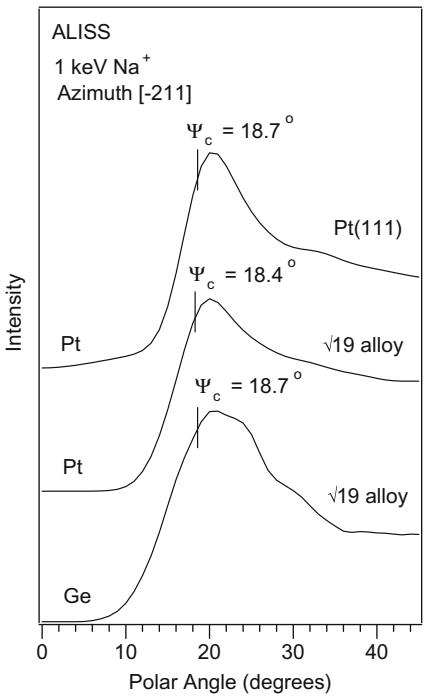

Fig. 10. Polar scans for first-layer Pt scattering features from Pt(111) and the $\sqrt{19}$ alloy and first-layer Ge scattering from the $\sqrt{19}$ alloy along the [−211] azimuthal direction. Critical angles ψ_c were calculated at 90% of the intensity maxima.

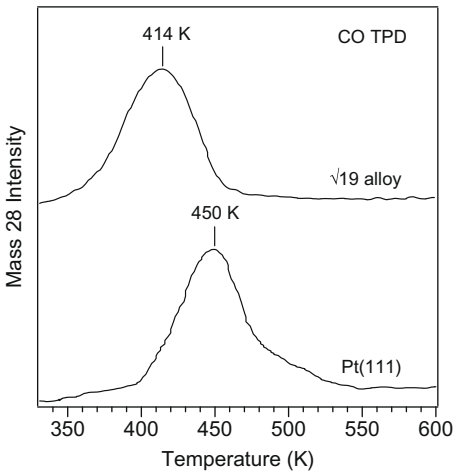

Fig. 11. CO TPD spectra after low CO exposures on Pt(1 1 1) and the $\sqrt{19}$ alloy at 325 K.

corrugation in a number of bimetallic surfaces with Sn alloyed into *fcc*(1 1 1) crystals, where an outward buckling of the larger Sn atoms in the vertical direction was induced, apparently cannot be extended to this system.

3.7. TPD

Fig. 11 shows TPD spectra of CO from Pt(1 1 1) and the $\sqrt{19}$ surface alloy. The CO TPD curves were obtained following a small exposure of 0.05-L CO on each surface that produced a low coverage of 0.1 ML of CO on Pt(1 1 1) at 325 K. The CO desorption peak on Pt(1 1 1) near 450 K can be assigned to the desorption of CO from atop sites [5,25,26]. On the $\sqrt{19}$ alloy, CO desorbs at lower temperatures in a peak near 414 K. This reduction of the CO-chemisorption energy has been attributed to the filling of the Pt *d*-band caused by *s*–*d* hybridization of the Ge *s* electrons and the Pt *d*-band [13,14]. Electron transfer from Ge to Pt *d* orbitals has been suggested also to explain the changes in activity and selectivity of Pt–Ge catalysts from those of pure Pt [2]. The lowering of the CO desorption temperature is similar to that observed in CO TPD spectra from ordered Sn/Pt(1 1 1) surface alloys [5].

NO TPD spectra (not shown) were obtained from Pt(1 1 1) and the $\sqrt{19}$ alloy following adsorption of 3-L NO on each surface. This dose gave a saturation coverage of NO on Pt(1 1 1) at 325 K. The desorption peak of NO near 364 K on Pt(1 1 1) is attributed to NO desorbing from bridge sites [6,27,28]. No adsorbs on the $\sqrt{19}$ alloy at 325 K. As for CO, the reduction of the NO adsorption energy was attributed to the reduction of *d*-hole density of the Pt surface induced by *s*–*d* hybridization in the alloy [13]. Lowering of the NO desorption temperature is similar to that observed for NO adsorbed on ordered Sn/Pt(1 1 1) surface alloys [6], but in these experiments we were unable to cool the crystal sufficiently to measure the NO desorption peak.

4. Conclusions

An ordered ($\sqrt{19} \times \sqrt{19}$)R23.4°-Ge/Pt(1 1 1) surface alloy was created by depositing a one-monolayer Ge film onto a Pt(1 1 1) surface at 300 K and subsequently annealing to 1000 K. This ordered structure was stable from 900 to 1200 K. The observed LEED pattern was assigned to two-domains of a *fcc*(1 1 1)-($\sqrt{19} \times \sqrt{19}$)R23.4° unit cell. STM images show that the unit-vector length for this superstructure of 12.1 Å is $\sqrt{19}$ times the unit-vector length of Pt (2.77 Å). STM images show chemical contrast and Ge atoms appear as bright spots. Quantitative analysis using ALISS establishes that the Ge surface concentration in this structure is 5.6 atom%. This is in excellent agreement with a value of 5.3 atom% predicted for a primitive ($\sqrt{19} \times \sqrt{19}$)R23.4° unit cell containing only one Ge atom. Two-domains of the ($\sqrt{19} \times \sqrt{19}$)R23.4° structure were observed in STM and LEED. ALISS polar scans establish that this structure is due to Ge atoms that are substitutionally incorporated into the Pt(1 1 1) surface rather than forming an ordered overlayer. Upon heating the monolayer thick Ge film to cause alloying, excess Ge atoms diffuse deep into the substrate so that a surface alloy is formed in which Ge atoms exist in the topmost layer with no significant concentration in the 2nd, 3rd, and 4th layers. This was confirmed by both XPD and ALISS polar scans. The Ge atoms in the surface layer are located at exactly the same positions as those of the replaced Pt atoms, without any buckling. The linear relationship between the lattice mismatch and surface corrugation from previous studies of Sn-transition metal alloys cannot be extended to this system. TPD results show that both CO and NO chemisorb more weakly on the Ge/Pt(1 1 1) alloy compared to the clean Pt(1 1 1) surface. This has been attributed previously to the *d*-band filling of Pt induced by *s*–*d* hybridization with Ge in the alloy.

Acknowledgments

This work was partially supported by the Analytical and Surface Chemistry Program in the Division of Chemistry, National Science Foundation.

References

[1] T. Komatsu, M. Mesuda, T. Yashima, Appl. Catal. A 194–195 (2000) 333.
[2] T. Komatsu, S.-I. Hyodo, T. Yashima, J. Phys. Chem. B 101 (1997) 5565.
[3] S.H. Overbury, D.R. Mullins, M.T. Paffett, B.E. Koel, Surf. Sci. 254 (1991) 45.
[4] Y. Li, B.E. Koel, Surf. Sci. 330 (1995) 193.
[5] M.T. Paffett, S.C. Gebhard, R.G. Windham, B.E. Koel, J. Phys. Chem. 94 (1990) 6831.
[6] C. Xu, B.E. Koel, Surf. Sci. 310 (1994) 198.
[7] Y.-L. Tsai, B.E. Koel, J. Phys. Chem. B 101 (1997) 2895.
[8] J.W. Peck, D.I. Mahon, D.E. Beck, B.E. Koel, Surf. Sci. 410 (1998) 170.
[9] C. Panja, B.E. Koel, J. Phys. Chem. A 104 (2000) 2486.
[10] C. Panja, N.A. Saliba, B.E. Koel, Catal. Lett. 68 (2000) 175.
[11] M. Batzill, D.E. Beck, B.E. Koel, Surf. Sci. 466 (2000) L821.
[12] K. Fukutani, Y. Murata, J. Brillo, H. Kuhlenbek, H.-J. Freund, M. Taguchi, Surf. Sci. 464 (2000) 48.
[13] K. Fukutani, T.T. Magkoev, Y. Murata, K. Terakura, Surf. Sci. 363 (1996) 185.
[14] K. Fukutani, T.T. Magkoev, Y. Murata, M. Matsumoto, T. Kawauchi, T. Magome, Y. Tezuka, S. Shin, J. Electron Spectrosc. Relat. Phenom. 88–91 (1998) 597.
[15] Y. Li, M.R. Voss, N. Swami, Y.-L. Tsai, B.E. Koel, Phys. Rev. B 56 (1997) 15982.
[16] S.H. Overbury, Y.-S. Ku, Phys. Rev. B 46 (1992) 7868.
[17] Y.-S. Ku, S.H. Overbury, Surf. Sci. 273 (1992) 341.
[18] C.-S. Ho, S. Banerjee, B.E. Koel, Surf. Sci., submitted for publication.
[19] C.-S. Ho, S. Banerjee, B.E. Koel, O.B. Duchemin, J.E. Polk, Appl. Surf. Sci. 252 (2006) 2657.
[20] R.G. Musket, W. McLean, C.A. Colmenares, D.M. Makowiecki, W.J. Siekhaus, Appl. Surf. Sci. 10 (1982) 143.
[21] A.T. Hubbard (Ed.), The Handbook of Surface Imaging and Visualization, CRC Press, Boca Raton, 1995.
[22] Y.G. Shen, D.J. O'Connor, K. Wandelt, R.J. MacDonald, Surf. Sci. 328 (1995) 21.
[23] H. Niehus, W. Heiland, E. Taglauer, Surf. Sci. Rep. 17 (1993) 213.
[24] D.P. Woodruff, T.A. Delchar, Modern Techniques of Surface Science, second ed., Cambridge University Press, Cambridge, 1994.
[25] H. Steininger, S. Lehwald, H. Ibach, Surf. Sci. 123 (1982) 264.
[26] P.R. Norton, J.W. Goodale, E.B. Selkirk, Surf. Sci. 83 (1979) 189.
[27] M.E. Bartram, B.E. Koel, E.A. Carter, Surf. Sci. 219 (1989) 467.
[28] B.E. Hayden, Surf. Sci. 131 (1983) 419.